

School of Natural Sciences and Mathematics

***Solar Influences on the Return Direction
of High-Frequency Radar Backscatter***

UT Dallas Author(s):

Angeline G. Burrell
Russell Stoneback

Rights:

©2018 American Geophysical Union. All Rights Reserved.

Citation:

Burrell, A. G., G. W. Perry, T. K. Yeoman, S. E. Milan, et al. 2018. "Solar Influences on the Return Direction of High-Frequency Radar Backscatter." *Radio Science* 53: 577-597, doi: 10.1002/2017RS006512

This document is being made freely available by the Eugene McDermott Library of the University of Texas at Dallas with permission of the copyright owner. All rights are reserved under United States copyright law unless specified otherwise.



Radio Science

RESEARCH ARTICLE

10.1002/2017RS006512

Key Points:

- e-POP RRI measurements of pulses from the Hankasalmi SuperDARN radar confirm the presence of a back lobe at all transmitted frequencies
- Seasonal and solar cycle variations are present in the radar's groundscatter return direction
- The groundscatter return direction is primarily influenced by variations in ionospheric plasma density

Correspondence to:

A. G. Burrell,
agb073000@utdallas.edu

Citation:

Burrell, A. G., Perry, G. W., Yeoman, T. K., Milan, S. E., & Stoneback, R. (2018). Solar influences on the return direction of high-frequency radar backscatter. *Radio Science*, 53, 577–597. <https://doi.org/10.1002/2017RS006512>

Received 28 NOV 2017

Accepted 17 MAR 2018

Accepted article online 23 MAR 2018

Published online 26 APR 2018

Solar Influences on the Return Direction of High-Frequency Radar Backscatter

Angeline G. Burrell¹ , Gareth W. Perry² , Timothy K. Yeoman³ , Stephen E. Milan³ , and Russell Stoneback¹ 

¹Department of Physics, University of Texas at Dallas, Dallas, TX, USA, ²Department of Physics and Astronomy, University of Calgary, Calgary, Alberta, Canada, ³Department of Physics and Astronomy, University of Leicester, Leicester, UK

Abstract Coherent-scatter, high-frequency, phased-array radars create narrow beams through the use of constructive and destructive interference patterns. This formation method leads to the creation of a secondary beam, or lobe, that is sent out behind the radar. This study investigates the relative importance of the beams in front of and behind the high-frequency radar located in Hankasalmi, Finland, using observations taken over a solar cycle, as well as coincident observations from Hankasalmi and the Enhanced Polar Outflow Probe Radio Receiver Instrument. These observations show that the relative strength of the front and rear beams is frequency dependent, with the relative amount of power sent to the front lobe increasing with increasing frequency. At the range of frequencies used by Hankasalmi, both front and rear beams are always present, though the main beam is always stronger than the rear lobe. Because signals are always transmitted to the front and rear of the radar, it is always possible to receive backscatter from both return directions. Examining the return direction as a function of local time, season, and solar cycle shows that the dominant return direction depends primarily on the local ionospheric structure. Diurnal changes in plasma density typically cause an increase in the amount of groundscatter returning from the rear lobe at night, though the strength of this variation has a seasonal dependence. Solar cycle variations are also seen in the groundscatter return direction, modifying the existing local time and seasonal variations.

1. Introduction

Coherent-scatter, high-frequency (HF), phased-array radars transmit signals between 3 and 30 MHz along narrow beams that are formed through constructive and destructive interference. The transmitted signals will return to the radar if they achieve perpendicularity to decameter-scale irregularities before they are absorbed by the ionosphere or travel past the ionospheric plasma density peak. Appropriate irregularities can be found in the *E* and *F* region ionosphere or on the ground. This second type of backscatter is known as groundscatter. The HF radar located at Hankasalmi, one of two Cooperative UK Twin Located Auroral Sounding System (CUTLASS) radars, commonly observes groundscatter returning from both in front of and behind the radar (Milan, Jones et al., 1997). This is a common occurrence for HF radars, especially those with log-periodic antennas, which have been shown to transmit signals and receive ground and ionospheric backscatter from both fields of view (Burrell et al., 2015).

The spatiotemporal distribution of backscatter depends on the structure of the medium that the radio signals travel through, as well as the strength of the signal and the presence of appropriate scattering targets. The high-latitude ionosphere can be highly structured, both vertically and horizontally, leading to complicated propagation paths. Ground-based radio propagation is primarily interested in the “bottomside,” consisting of the ionosphere up to the height of the plasma density peak. There may be up to four distinct regions making up the bottomside ionosphere at Earth: the *D*, *E*, *F*₁, and the lower portion of the *F*₂ region. The *D*, *E*, and *F*₁ regions coincide with ion production peaks caused by photoionization at different wavelengths, while the *F*₂ peak is formed by balancing plasma transport and production. Horizontal structures in the ionosphere are primarily created by changes in the solar zenith angle, the geomagnetic field, and the neutral atmosphere. One relevant example is the midlatitude trough, which forms near 00:00 magnetic local time (MLT) in the *F* region ionosphere during the winter. The midlatitude trough is characterized by a localized plasma density enhancement in the auroral oval with densities that can exceed daytime values, a density depletion equatorward of this enhancement that lends the phenomenon its name, and a second,

more gradual, density enhancement at lower midlatitudes (e.g., Scali, 1992; Yang et al., 2015; Werner & Pröls, 1997). Horizontal density gradients such as the midlatitude trough may either benefit or hinder propagation conditions. Initial backscatter statistics at the CUTLASS radars showed diurnal and seasonal changes in the backscatter occurrence rate and location, which were tied to changes in the *E* and *F* region ionospheric plasma density (Milan, Yeoman et al., 1997).

The availability of appropriate scattering targets will also affect when backscatter is observed and where it returns from. Although this study is concerned with groundscatter, not all ground surfaces are consistently viable groundscatter targets. For example, the availability of quality targets on the ocean will diminish in the presence of sea ice (Ponomarenko et al., 2010; Shand et al., 1998). While the current study is not concerned with the variability of the quantity of groundscatter, the influence of significant quantities of sea ice in only the front field of view on the preferred groundscatter return direction is considered.

This article examines the return direction of groundscatter observed at the Hankasalmi HF radar for quiescent ionospheric conditions in response to diurnal, seasonal, and solar cycle variations. The instrumental influences on return direction, including the relative strengths of the front and rear beams, are also explored. Analysis of the groundscatter return direction, interpreted with the assistance of the ionospheric plasma density and signal strength observations, demonstrates that when it is possible to receive backscatter from both fields of view, the dominant return direction is that which contains a higher signal-to-noise ratio, as well as smoother variations in and more suitable level of ionospheric plasma density, rather than simply the stronger transmitted signal.

2. Data

Several data sets were used in this study. The principal data set consists of backscatter observed from the HF radar at Hankasalmi, one of the radars in the Super Dual Auroral Radar Network (SuperDARN; Chisham et al., 2007; Greenwald et al., 1995). This network of HF radars was established to observe the midlatitude and high-latitude ionosphere over the North and South Poles. The Hankasalmi radar, which consists of two arrays of log-periodic antennas, was built and is administered by the University of Leicester. The main array consists of 16 antennas (separated by 15 m) that both transmit and receive signals. The second array is for interferometry and consists of four antennas that only receive data. The Hankasalmi radar is located at 62.32°N, 26.61°E, with a forward field of view that extends north (centered 12° counterclockwise from geographic north) for 75 range gates (where each range gate is typically 45 km) and spans 16 beams azimuthally (where each beam is separated by 3.24°); the rear field of view mirrors the front field of view, extending southward with a center 12° counterclockwise from geographic south. Signals sent out from the radar range between 0° and 35° elevation. The Hankasalmi radar has operated continuously since February 1995, making it possible to explore the behavior of radar backscatter as a function of local time, season, and solar cycle. Details of the SuperDARN data analysis are presented in section 2.1.

Secondary data sets are used to select appropriate periods of study and interpret the behavior of the groundscatter observed at Hankasalmi. These data sets include the Enhanced Polar Outflow Probe Radio Receiver Instrument (e-POP RRI; James et al., 2015), Global Positioning System (GPS) vertical total electron content (VTEC; Rideout & Coster, 2006), snow cover and sea ice extent (Brodzik & Armstrong, 2017), and several solar and geomagnetic indices. These data sets are presented in section 2.2.

2.1. SuperDARN Data Analysis

The raw SuperDARN backscatter was processed to obtain phase lag—the difference in the signal phase measured at the main and interferometer arrays that is used to calculate the elevation angle—(Ψ_0), backscatter power—or signal-to-noise ratio—(P), line-of-sight velocity (v), and spectral width (w) using FITACF version 2.0, the standard routine used to process (or fit) the SuperDARN autocorrelation functions (Ponomarenko & Waters, 2006). This version avoids the issues discarding good lags that has been documented in FITACF version 2.7 (Ponomarenko, 2017). Once the fitted parameters were obtained, a second level of processing was performed to reduce the error in elevation angle (which is needed to determine the location of the scattering target) by removing the frequency-dependent phase delay (Burrell et al., 2016; Ponomarenko et al., 2015) and determining the return direction (Burrell et al., 2015), as well as reducing instances of slow-moving ionosphere backscatter within the groundscatter data set. Figure 1 illustrates these steps for an 11-hr period at Hankasalmi. Panels (a) and (b) reproduce the middle two rows of Figure 14 in Burrell et al. (2015) and show the backscatter as a function of universal time (UT), range gate, and power in front of and behind the radar,

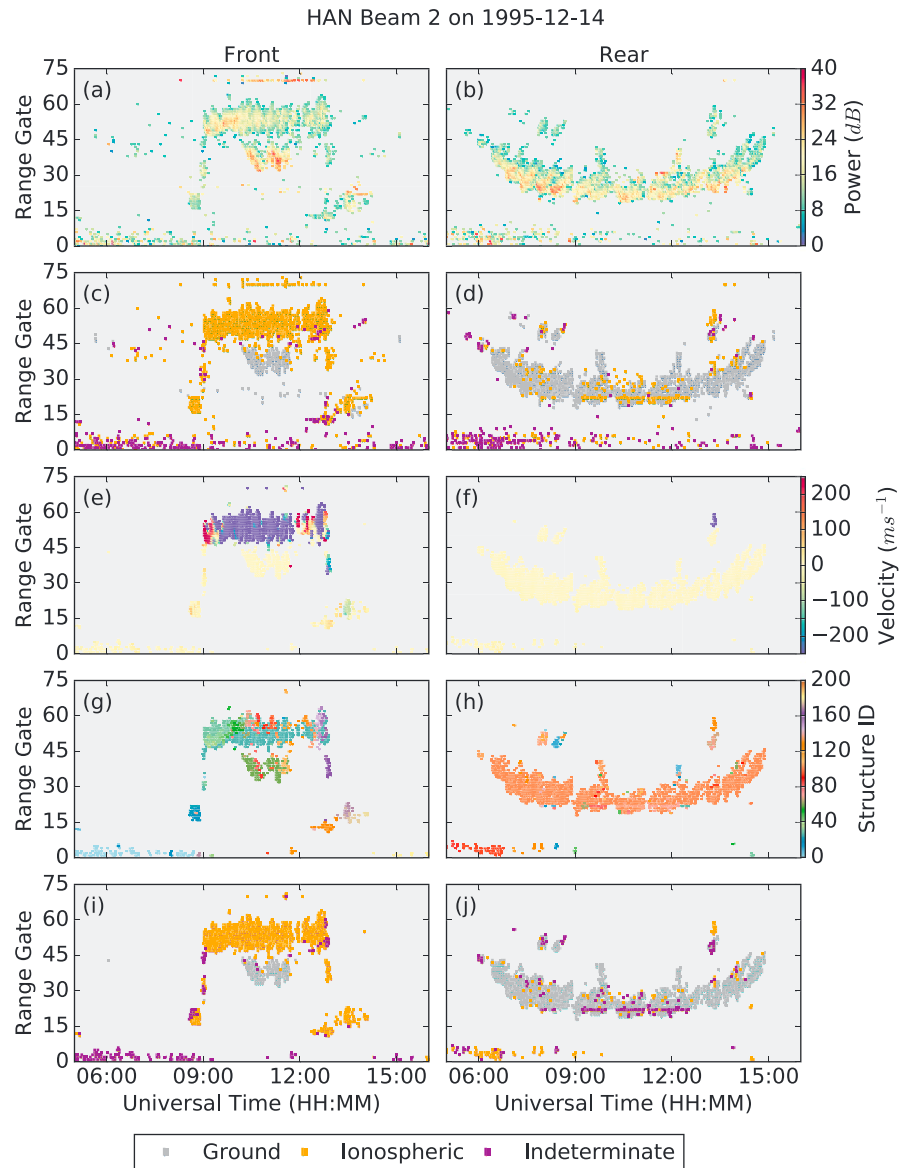


Figure 1. Backscatter observed by Hankasalmi on 14 December 1995 along beam 2 grouped by field of view (front in the left column and rear in the right column) for four different processing steps. Panels (a)–(d) show the backscatter with successfully determined return directions, standard ionospheric backscatter, updated groundscatter, and indeterminate backscatter that has been removed from the groundscatter data set. Panels (e)–(h) illustrate the intermediate steps taken to identify slow-moving ionospheric backscatter, with panels (e) and (f) showing the median Doppler velocities and panels (g) and (h) showing backscatter structures formed using a depth-first search. Panels (i) and (j) show the final backscatter assignments into ground, ionospheric, and indeterminate categories based on the percentage of fast points within each backscatter structure.

respectively. The small differences between Figures 1a and 1b and Figure 14 in Burrell et al. (2015) are due to improvements in phase calibration. Figures 1c–1j illustrate the steps taken to improve the separation of ground and ionospheric backscatter. Once the groundscatter data set is cleaned, the characteristics of the propagation path are obtained and the statistical analysis is performed.

Groundscatter is typically distinguished from ionospheric backscatter by using v and w to identify slow-moving backscatter with a narrow distribution of velocities.

$$|v| + \frac{1}{3}|w| < 30 \text{ m/s} \quad (1)$$

This criterion, however, was developed to ensure a clean set of ionospheric backscatter observations and so misidentifies a significant amount of slow-moving ionospheric backscatter and meteor scatter (Blanchard et al., 2009; SuperDARN Data Analysis Working Group Participating members et al., 2018). Because this study examines groundscatter, it is necessary to apply additional criteria on top of the standard criterion (equation (1)) to obtain a groundscatter data set that is not contaminated with slow-moving ionospheric backscatter or meteor scatter. This is accomplished by assessing the power, slant distance, and nearby backscatter for signals returning along a single beam, as well as evaluating the characteristic speed of large spatially and temporally connected groups of backscatter.

Conditions for the former requirement are outlined in the list below. Backscatter that meet the following conditions are removed from the groundscatter data set and placed in a third “indeterminate” data set. For the purposes of determining the backscatter return direction, indeterminate backscatter is treated as ionospheric backscatter.

1. $d < 78$ km: The slant distance, d , must be high enough to reach the ionosphere (only applicable in some special operating modes).
2. $P < 0$ dB: P must be positive.
3. $(rg < 10) \wedge (P < 5$ dB): Establish a lower limit for P near the radar, where only the high-power groundscatter near the skip distance (first range gate, rg , where groundscatter is seen) will be observed.
4. $\frac{N_g}{N_{tot}} < 50\%$: The number of groundscatter points (N_g) must make up at least half of the total number of backscatter points (N_{tot}) in a 10 range gate window centered at the location of each groundscatter observation.

Figures 1c and 1d illustrate how these criteria perform for the example period at Hankasalmi. Two clear ionospheric backscatter structures are shown in orange in front of the radar: a short-lived group of $\frac{1}{2}$ -hop backscatter near range gate 20 at 08:30 UT and a long-lived group of $1\frac{1}{2}$ -hop backscatter near range gate 50 between 09:00 and 13:00 UT. There are also two 1-hop groundscatter structures, shown in gray and centered at 11:00 UT, which form the characteristic “U” shape caused by the rise and fall of plasma production associated with the length of the day. The one in front of the radar lasts from 10:00 to 12:00 UT, while the one behind the radar stretches from about 06:00 to 15:00 UT. The duration of each of these structures reflects the different lengths of daylight at their respective latitudes. At the nearest range gates, the abundant indeterminate (purple) and ionospheric backscatter can be attributed to meteor ablation (Hall et al., 1997). There are also several backscatter structures that contain significantly mixed populations of ground, indeterminate, and ionospheric backscatter (e.g., the structure seen in front of the radar between 12:00 and 14:00 UT near range gate 15), as well as some ionospheric backscatter strewn throughout the large “U” of groundscatter returning from behind the radar. The listed criteria successfully remove near-range ionospheric backscatter (including meteor ablation) from the groundscatter data set but only identify a portion of the slow-moving ionospheric backscatter. Thus, further processing is needed to produce clean groundscatter and ionospheric backscatter data sets.

It is possible to identify slow-moving ionospheric backscatter by considering the fraction of fast- and slow-moving measurements made within spatially and temporally connected groups of backscatter. Ribeiro et al. (2011) developed a method to find slow-moving ionospheric backscatter in the groundscatter data set. Their method median-filtered the Doppler velocity using a 3 beam \times 3 range gate \times 3 scan boxcar, searched for backscatter structures (groups of points connected by adjacent range gates or scans), and evaluated the relative fraction of fast- and slow-moving backscatter within each structure using empirically determined thresholds based on the temporal duration of each structure. This study adapts their method, allowing backscatter structures to span multiple beams and creating additional criteria for groundscatter and short-lived ionospheric backscatter structures.

The first step, median filtering the Doppler velocity, is shown in Figures 1e and 1f. Comparing panels (e) and (f) to panels (c) and (d) reveals that some of the backscatter has been removed (alternatively, compare any of panels (e), (g), and (i) to panel (c) and panels (f), (h), and (j) to panel (d); no backscatter is removed in the subsequent steps, but the colors of all points are easier to see). This happens because a minimum threshold of at least six backscatter observations per boxcar was required to compute a median. The low threshold was chosen to minimize the impact of the median filter on backscatter measured by the first and last beams, or near the first and last range gates. The removal of isolated backscatter instances is viewed as beneficial, since it consists primarily of noise and echoes from meteor ablation (Ribeiro et al., 2011; Ruohoniemi & Baker, 1998).

The results of the second step, identifying backscatter structures, are shown in Figures 1g and 1h. Following the approach of Ribeiro et al. (2011), a depth-first search was used to identify and group together neighboring backscatter. The analysis here differs by allowing the search to span multiple beams (permitting structures an azimuthal as well as temporal extent) and considering the virtual height of the backscatter when identifying neighbors. Thus, the backscatter in each structure shown in Figures 1g and 1h shares the same radar program mode, transmission frequency, and return direction, differing from their nearest neighbors by no more than one beam, one range gate, one scan time, and 15 km in virtual height. It is possible to use the virtual height in this analysis because the elevation angles have been calibrated.

Next, the possibility that each backscatter structure is made up of ionospheric backscatter is tested. The criteria used to identify ionospheric backscatter are the same as those used by Ribeiro et al. (2011) with one exception: ionospheric backscatter that is observed for an hour or less is not removed, since short-lived irregularities can occur. Instead, backscatter patches that last an hour or less are required to contain a majority (more than half) of fast backscatter to be flagged as ionospheric. Any backscatter that is not flagged ionospheric is flagged as indeterminate unless more than half of the backscatter has been flagged as groundscatter (in which case it is flagged as groundscatter). The results of this analysis are shown in Figures 1i and 1j.

Comparing Figures 1c and 1d to Figures 1i and 1j reveals how the processing steps outlined above compare to the standard groundscatter detection method (equation (1)), which groups the gray groundscatter and purple indeterminate backscatter together. Focusing on the rear field of view, panels (d) and (j) show that most of the ionospheric backscatter in the large groundscatter structure has been moved into the indeterminate data set. These points could not be moved into the groundscatter data set because their virtual heights differed too much from the surrounding groundscatter; flagging this data as indeterminate thus improves both the ground and ionospheric backscatter data sets. There are also instances where slow-moving ionospheric backscatter is identified. Comparing panels (c) and (i) shows that the ionospheric backscatter structure seen after 12:00 UT between range gates 15 and 30 by beam 2 was originally about half groundscatter and half ionospheric backscatter. After application of the four criteria that define indeterminate backscatter, most groundscatter observations in this patch were reflagged as indeterminate. The remaining processing steps revealed that the backscatter in this patch is predominantly fast and so was reflagged as ionospheric.

This analysis creates a clean set of groundscatter with reliable elevation angles, which have been used to determine the location of the ground scattering targets by assuming straight-line propagation paths. The assumption of a triangular (where the triangle is formed by the straight path up from the radar to the ionospheric refraction point, the straight path down to the ground scattering target, and the ground distance back from the scattering target to the radar) instead of a refracted propagation path (where the ionosphere bends the transmitted signal from a straight path away from the radar toward and then past the horizontal, until it returns back down to the ground) introduces an error into the calculated altitude. This means that the true distance lies further from the radar than the calculated distance reflects (e.g., Chisham et al., 2008). Close to the radar this error is negligible, while the error for backscatter returning from the furthest measured distances is typically about 60 km (Yeoman et al., 2001). This study uses the geographic locations of groundscatter returns to understand the role that the availability of scattering targets and the local ionospheric plasma density play in determining the amount and location of groundscatter observations. Longer-term variations examine only the groundscatter return direction.

Magnetic coordinates are calculated from the geographic locations using Altitude-Adjusted Corrected Geomagnetic coordinates-Version 2 (Shepherd, 2014). Two regions about magnetic noon and midnight were selected, each including all data with MLTs within 1 hr of noon or midnight. Seasons consist of 1 month of data, namely the month that contains a solstice or equinox. All data were obtained from times when a common mode was used. These modes scan across all beams every 1 or 2 min and have range gates of 45 km.

2.2. Secondary Data Sets

2.2.1. Enhanced Polar Outflow Probe Radio Receiver Instrument

This work uses e-POP RRI to analyze the power profile of the transmissions from the Hankasalmi SuperDARN radar. e-POP is the scientific payload on the CASCade, Smallsat, and IONospheric Polar Explorer (CASSIOPE) spacecraft (Yau & James, 2015), which was launched into an elliptical, polar orbit with an inclination of 81° on 29 September 2013. At launch its perigee and apogee were approximately 325 and 1,300 km, respectively,

and have changed (as of March 2018) to approximately 340 and 1,310 km as a result of atmospheric drag. RRI, one of eight e-POP instruments, is a digital radio receiver for studying natural and artificial radio waves between 10 Hz and 18 MHz (James et al., 2015).

RRI has four 3-m monopole antennas, which were electronically configured into a crossed-dipole mode to provide polarimetry measurements of incident radio waves. RRI samples at a rate of 62.5 kHz across a passband of 30 kHz, which is sufficient to fully resolve and study SuperDARN pulses (300 μ s in length) and their constituent magnetoionic propagation modes (cf. Perry et al., 2017). RRI's high sampling rate generates a large amount of data that prevent it from being operated continuously. Thus, RRI is operated in a "campaign"-like manner, with experiments planned several days in advance. In the case of coordinated experiments with ground instruments such as radars, this ensures that the transmissions from the targeted radar are within RRI's receiving passband.

RRI's digital electronics package allows the instrument to be tuned in an agile manner. In the crossed-dipole mode, the RRI dipoles can be programmed separately or similarly. Either dipole can be fixed to sample in a particular band or repetitively swept through a band of frequencies in a short period of time. Five experiments were arranged between RRI and the SuperDARN radar at Hankasalmi: 6 July 2016, 11 August 2016, 26 March 2017, 2 April 2017, and 23 April 2017. During these experiments, RRI used a linear sweep mode, cycling repetitively through 8.31, 9.96, 11.61, 13.26, 14.91, and 16.56 MHz. RRI dwelled on each frequency for 0.167 s (taking 1 s for the entire cycle). Meanwhile, Hankasalmi was programmed to transmit at 9.955, 13.255, and 16.555 MHz for all five experiments, cycling through those frequencies every 2 s. Radio spectrum allocations prevented Hankasalmi from transmitting in all of RRI's tuned bands. The radar was operated in "stereo mode," wherein two frequencies are transmitted and received by the system simultaneously. The results of these experiments and their implications are discussed in section 3.

2.2.2. Global Positioning System Vertical Total Electron Content

The state of the ionosphere over Hankasalmi is determined through column-integrated measurements of the electron density, namely, GPS VTEC (Rideout & Coster, 2006). This study uses VTEC that was smoothed using a $3^\circ \times 3^\circ$ geographic latitude \times longitude boxcar median to provide data at a 1° resolution in geographic latitude and longitude. The filtered VTEC was then matched to the nearest beam and range gate, allowing the likelihood of SuperDARN groundscatter detection to be related to the plasma density between the radar and the groundscatter reflection point.

2.2.3. Northern Hemisphere Snow Cover and Sea Ice

The availability of groundscatter reflection targets in the sea near polar coastlines is known to be affected by the sea ice extent. In this study, the Northern Hemisphere Equal Area Scalable Earth Grid 2.0 weekly snow cover and sea ice extent data set was used to determine areas affected by sea ice (Brodzik & Armstrong, 2017). Each grid cell is 25 km \times 25 km. The sea ice data for this study were measured using the Defense Meteorological Satellite Program Special Sensor Microwave Imager passive microwave instrument (Alishouse, 1991), and contain the weekly averages of sea ice. A positive sea ice detection is made when more than 15% of the observations made in a grid cell observed sea ice (Johannessen et al., 1996).

2.2.4. Solar Activity

Solar activity is measured using the galactic cosmic ray count (CR) measured at Oulu, Finland (Usoskin et al., 2001) and the 10.7 cm radio flux ($F_{10.7}$; Cortie, 1912). Galactic cosmic rays are atomic nuclei without any electrons that originate from sources outside the solar system and are observed almost uniformly over the surface of the Earth. This radiation is deflected by strong magnetic fields; this is useful since the interaction between galactic cosmic rays and the interplanetary magnetic field causes a solar cycle variation in the quantity of galactic cosmic rays that reach Earth. This means that at high levels of solar activity, fewer galactic cosmic rays will be measured at Oulu, while at low levels of solar activity, many galactic cosmic rays will be measured there (Cane et al., 1999). $F_{10.7}$, on the other hand, increases with increasing solar activity and is a commonly used proxy for solar extreme ultraviolet (EUV) irradiance. The relationship between solar EUV irradiance and $F_{10.7}$ has been shown to deviate at very low levels of solar activity (Liu et al., 2011, and references therein), but these conditions were not encountered during the 23rd solar cycle. The $F_{10.7}$ index was obtained from the National Oceanic and Atmospheric Administration/Space Weather Prediction Center. Both of these measures of solar activity are used to examine variations in the groundscatter propagation over the 23rd solar cycle.

2.2.5. Geomagnetic Activity

The polar ionosphere is highly responsive to changes in the magnetosphere. To reduce the influence of magnetosphere-ionosphere coupling on this study, one further constraint was placed upon the data. Geomagnetically quiet periods were selected by requiring an $A_p \leq 22$, ensuring that geomagnetic disturbances do not interfere with the interpretation of local time, seasonal, and solar cycle variations. The A_p was obtained from the National Aeronautics and Space Administration/Goddard Space Flight Center OMNI data set through OMNIweb. The only exception to this condition is the coordinated experiment between e-POP RRI and the Hankasalmi SuperDARN radar on 23 April 2017, which is discussed in more detail in section 3

3. Front and Rear Signal Strength

Understanding the relative strength of the signal sent to the front and rear of the radar (the front and rear lobes), and how these strengths may change with frequency, is necessary when interpreting the variations in backscatter return direction. The strength of the rear lobe depends on the radar transmission frequency, antenna hardware, and various environmental conditions. The complexity and transient nature of many of these conditions, coupled with limits on aerial observations, have made it difficult to construct a realistic model of the Hankasalmi radar lobes. Coordinated observations of the Hankasalmi signals by e-POP RRI have made it possible to examine the relative strengths of the front and rear lobes at several different frequencies.

Results of coordinated experiments between e-POP RRI and the Hankasalmi SuperDARN radar are plotted in Figure 2. In the top row, the ground tracks of the CASSIOPE satellite during the experiment are plotted in panel (a), along with the beams used in these experiments. Panels (b) and (c) show the elevation and bearing angles of the spacecraft with respect to Hankasalmi. The range of the elevation angle parameter is $0^\circ - 180^\circ$, where 0° is directed to geographic north and parallel to the geographic meridian at Hankasalmi. The measured power of the radar pulses extracted from the data stream of RRI Dipole 1 are plotted in Figures 2d–2f and 2g–2i, with respect to the elevation and bearing angle of the spacecraft, respectively, and sorted by RRI's tuning frequency.

The radar pulses plotted in Figures 2d–2i were extracted from RRI's received signal using the matched filter technique described in Perry et al. (2017). The received power of each pulse was estimated using Ohm's law: $P = V^2/Z_0$, where V is the voltage measured by RRI Dipole 1 and $Z_0 \approx 377 \Omega$ is the impedance of free space. The estimated power was then mapped back to Hankasalmi, with the assumption that it decreased as the inverse of the line-of-sight separation distance between the radar and spacecraft, squared. Variations in the orientation of the spacecraft, and therefore the normal of the RRI dipole plane during the experiments, were also accounted for. It is important to note that this technique assumes straight-line propagation paths with pulses on each frequency band that were equivalent to one another. This was certainly not the case in reality; for example, the geometric path lengths of the pulses would have increased as a function of decreasing transmitting frequency as a result of refraction. Nevertheless, this technique provides a first-order evaluation for investigating the power profiles of the Hankasalmi SuperDARN radar.

The received power profiles in Figures 2d–2i exhibit the expected power profile for the SuperDARN Hankasalmi radar system (cf. Figure 1 in Milan, Jones et al., 1997). The most notable feature is the peak power in the front lobe, directed to the north, which is constrained to a narrow beam in the range of $10^\circ - 20^\circ$ in elevation and $335^\circ - 350^\circ$ in bearing. Both are consistent with inbound spacecraft trajectories aligned with Hankasalmi's beams. During the experiment, the Hankasalmi radar only transmitted on the beams that covered the vicinity of CASSIOPE's ground track in the front field of view. For all of the experiments except for 23 April 2017, Hankasalmi transmitted on beams 4, 5, 6, and 7 (using 0–15 beam indexing). On 23 April 2017, Hankasalmi transmitted on beams 3, 4, 5, and 6.

A front-to-back power ratio ($F_p:R_p$) estimate was attempted for each experiment. However, due to a lack of received radar pulses from behind the Hankasalmi radar, only four out of 15 of the possible $F_p:R_p$ estimates (corresponding to the 16 July and 11 August 2016 experiments) could be made. In Figure 2a, the CASSIOPE tracks for those experiments intersect both the front and back lobes of the transmitting beams, whereas the tracks from the other three experiments do not intersect the back lobes. Since the radar's power in regions outside of the main front and rear lobes is expected to be suppressed (cf. Figure 1 in Milan, Jones et al., 1997), it is not surprising that insufficient pulses were detected to calculate $F_p:R_p$ for those experiments. Nevertheless, it is clear from these estimates that the $F_p:R_p$ is large and generally consistent with what is expected from

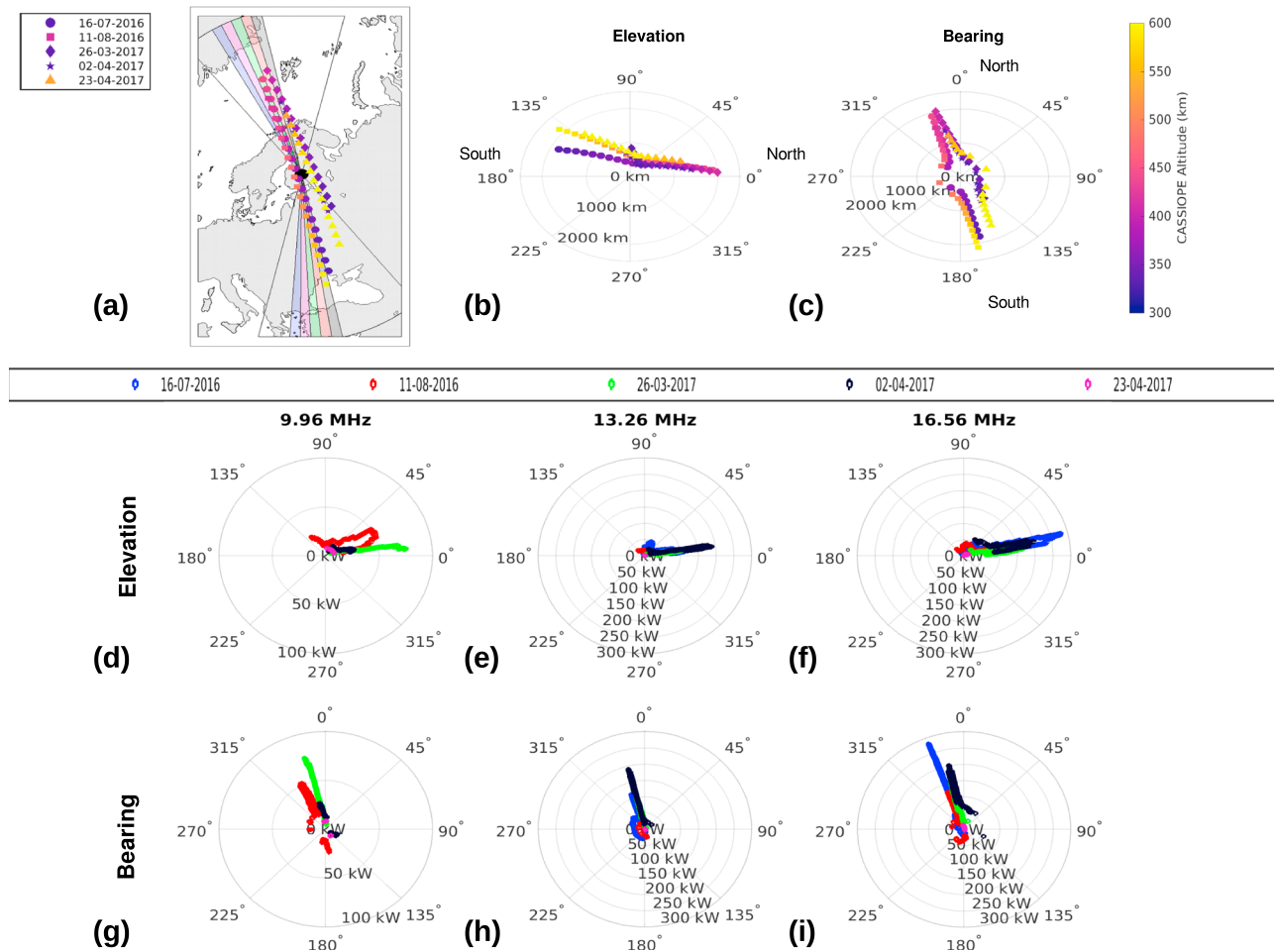


Figure 2. Results of five experiments between Radio Receiver Instrument (RRI) and the Hankasalmi Super Dual Auroral Radar Network (SuperDARN) radar. Panel (a) shows CAsCade, Smallsat and IOnospheric Polar Explorer (CASSIOPE)'s ground track, color coded by the spacecraft altitude, with Hankasalmi's location marked with a black circle. This panel also shows Hankasalmi's front and rear fields of view and highlights the beams used in these experiments: beams 3 (blue), 4 (magenta), 5 (green), 6 (red), and 7 (black). Panels (b) and (c) show polar plots of the elevation and bearing tracks of CASSIOPE's location with respect to Hankasalmi (also color coded by spacecraft altitude). The radial tick marks correspond to the line-of-sight range between Hankasalmi and CASSIOPE during a given experiment. The received power of SuperDARN pulses extracted from the RRI data stream are shown in polar plots with respect to elevation (d–f) and bearing (g–i) for 9.96 (left column), 13.26 (middle column), and 16.56 MHz (right column). These traces are color coded by date.

theoretical modeling (Milan, Jones et al., 1997; Sterne et al., 2011). The exact experiment times, $F_p:R_p$ for each frequency, and trace color from Figure 2 are shown in Table 1. Despite the limited sampling, the $F_p:R_p$ appears to be highest at 16.56 MHz (12–23 dB) and lowest at 9.96 MHz (11 dB). As a point of comparison, Sterne et al. (2011) modeled the $F_p:R_p$ to be 14.72 dB for a SuperDARN radar composed of a log-periodic array, an array construction that is similar to the Hankasalmi radar, transmitting at 14 MHz. The number of blank cells in Table 1 speaks to the difficulty in constructing a power profile for HF radar from spacecraft measurements. Elaborating on the differences between the modeling and measurements for multiple SuperDARN radars with e-POP RRI is underway as part of a separate study. The current measurements show that most of Hankasalmi's power is directed to the front, with a smaller, yet nonnegligible, amount of power directed in the rear lobe. The $F_p:R_p$ increases with increasing frequency.

Another important property of the profiles in Figures 2d–2i is the relationship between the power of the pulses received by RRI and Hankasalmi's transmission frequency: the received power increased with transmitting frequency. At higher frequencies, the ray paths of the radar's transmissions are less affected by interaction between the radar pulses and the magnetoplasma. Therefore, less refraction and dispersion occurs at higher frequencies, which results in an increased power signature at CASSIOPE's location. Lastly, radio wave absorption is inversely proportional to the square of the carrier frequency of a propagating radio wave

Table 1
e-POP RRI/Hankasalmi Experiment Times and Front-to-Rear Power Ratios

Date	Time (UT)	$F_p:R_p$ (dB)			Figure 2 line color
		9.96 MHz	13.26 MHz	16.56 MHz	
16 July 2016	13:31:15–13:39:11	–	11.5	23	Blue
11 August 2016	10:08:14–10:16:11	11	–	12	Red
26 March 2017	03:08:13–03:14:10	–	–	–	Green
2 April 2017	02:19:13–02:24:10	–	–	–	Black
23 April 2017	23:24:14–23:30:11	–	–	–	Pink

(Hargreaves, 1994). Therefore, it is expected that the received power will decrease as Hankasalmi’s transmitted frequency decreases, as demonstrated in Figures 2d–2i.

An important feature to point out in Figure 2 is that RRI received very few pulses on 23 April 2017. Additionally, the power of the pulses that are present are severely attenuated compared to pulses received on other days. At the time of this experiment, the A_p index was 32, indicating heightened geomagnetic activity. Therefore, the lack of received pulses and their attenuated power may be a result of geomagnetic conditions. All of the other e-POP RRI experiments with Hankasalmi occurred during times when the A_p was below 22.

The data displayed in Figure 2 have important implications when considering the origin of radar echoes measured by Hankasalmi and other coherent-scatter HF radars in general. Even though the majority of Hankasalmi’s power is directed forward (northward), a nonnegligible amount is directed backward (southward). Furthermore, the power radiated into the rear lobe varies with transmitting frequency. As Figure 2 shows, the power received by RRI in Hankasalmi’s rear lobe at 16.56 MHz is of the order of the power received in the front lobe at 9.96 MHz. As will be shown in section 4, the high $F_p:R_p$ measured by RRI does not preclude the detection of groundscatter in the rear lobe. Figure 2 shows that the signal-to-noise ratio of those echo returns will be reduced, rather than eliminated.

4. Groundscatter Distribution

With the understanding that groundscatter may return from both in front of and behind the Hankasalmi radar, it remains to be determined how often and why groundscatter is seen in each field of view. This study begins by examining the solar activity variations in groundscatter over the 23rd solar cycle, as shown in Figure 3. The top row shows solar activity levels, with $F_{10.7}$ in panel (a) and CR in panel (b), while the bottom row shows the groundscatter counts. The number of groundscatter points returning from behind the radar are shown in red, and the number returning from the front are shown in yellow. These bars are placed next to each other

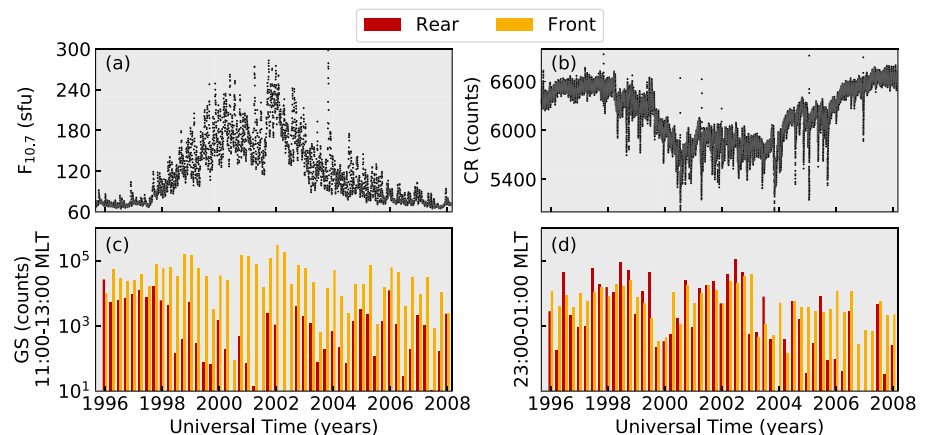


Figure 3. Solar cycle variations in $F_{10.7}$ (a), cosmic ray (CR) (b), and groundscatter (GS) counts at noon (c) and midnight (d) magnetic local time (MLT) observed at Hankasalmi. The red bars show the GS counts returning from behind the radar, and the yellow bars, alongside the red bars, show the GS counts returning from in front of the radar. Note that the GS counts are shown on a logarithmic scale.

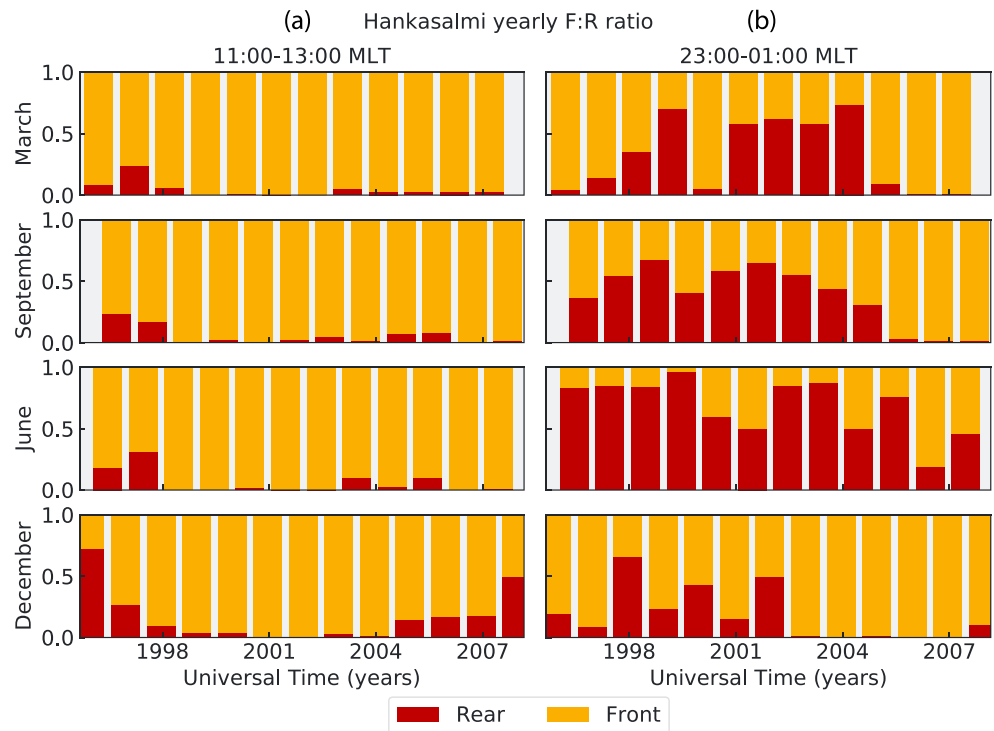


Figure 4. Ratio of groundscatter returning from the front (yellow) and rear (red) fields of view for each season and magnetic local time (MLT) sector as a function of universal time. Magnetic noon is shown in column (a), and magnetic midnight is shown in column (b). Each row shows a season centered at March, September, June, and December (ordered from top to bottom).

and together give the total number of groundscatter points for that year and season. The groundscatter counts for magnetic local noon are shown in panel (c) and magnetic midnight in panel (d). This figure shows that each year and season has hundreds to several hundred thousand groundscatter detections. However, such detections are not always available from both fields of view. There are several years in both MLT sectors that detected groundscatter only returning from in front of the radar. As discussed in section 2.1, the data have been down-selected by program mode, times when interferometer calibration were possible, and geomagnetic activity level; thus, they represent a similar set of instrumental and geophysical conditions rather than the total amount of groundscatter observed at Hankasalmi.

A clearer picture of the yearly variations in the relative amount of groundscatter returning from each field of view for every season and MLT sector is presented in Figure 4. This figure shows the ratio of groundscatter detected from in front (yellow) and behind (red) the radar ($F:R$) as a function of year during the 23rd solar cycle. Magnetic noon is shown in column (a) and magnetic midnight in column (b). Seasons are ordered from top to bottom, with equinox on top (March and September) and solstice on the bottom (June and December). The temporal variations are strongest during solstices. In December, a solar cycle variation is clearly seen at noon. In June, a diurnal variation dominates, with groundscatter predominantly returning from the front at noon and the rear at midnight. Both equinox months behave similarly; they are dominated by a diurnal variation like that seen during the June solstice.

While annual changes in the groundscatter $F:R$ can be used to explore solar cycle variations, there is no need to do so when solar cycle indices are available. Figures 5 and 6 have the same format as Figure 4, but show the groundscatter detection $F:R$ as functions of $F_{10.7}$ and CR count, respectively. As expected from Figure 4, the noon December $F:R$ increases with increasing solar activity as measured by both the $F_{10.7}$ and the CR counts. The amount of groundscatter returning from behind the radar is over 50% at low levels of $F_{10.7}$ and almost reaches 50% at times with high CR counts. In both figures, the $F:R$ quickly decreases as solar activity increases.

At midnight in December, no clear solar cycle variation is present. This is also the case for both MLT sectors during the June solstice and both equinoxes at noon. At midnight in March and September, however,

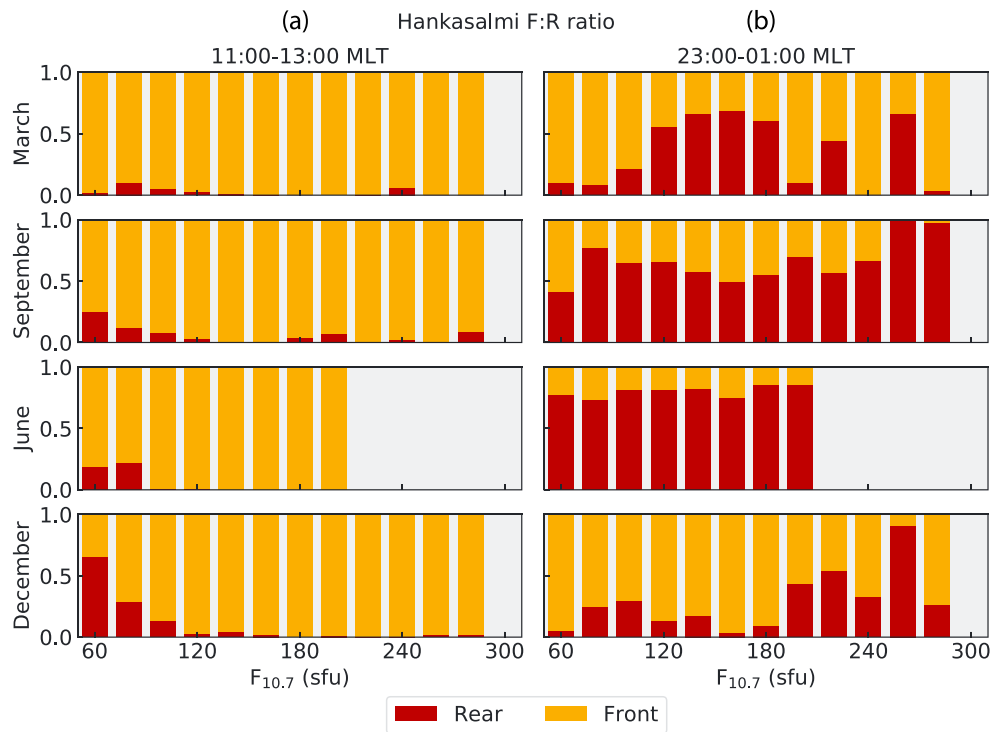


Figure 5. Ratio of groundscatter returning from the front and rear fields of view for each season and magnetic local time (MLT) sector as a function of $F_{10.7}$. (a) 11:00–13:00 MLT. (b) 23:00–01:00 MLT.

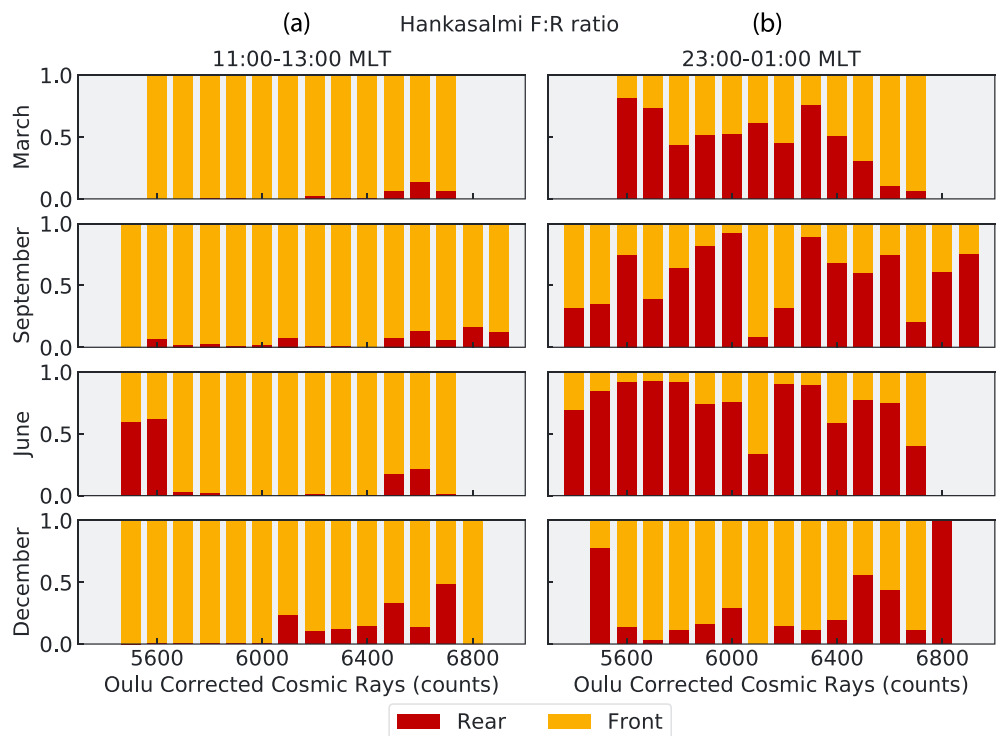


Figure 6. Ratio of groundscatter returning from the front and rear fields of view for each season and magnetic local time (MLT) sector as a function of cosmic ray count. (a) 11:00–13:00 MLT. (b) 23:00–01:00 MLT.

there does appear to be a small solar cycle variation in the $F:R$ that shows more groundscatter returning from behind the radar at higher levels of solar activity. The midnight March sector shows an increasing $F:R$ with increasing CR count (decreasing solar activity) in Figure 6, which is largely mirrored by the $F_{10.7}$ in Figure 5.

Possible reasons behind these MLT, seasonal, and solar cycle variations include the influence of the ionosphere on propagation paths, changes in the properties of the scattering surfaces that alter the availability of groundscatter targets, and changes in transmission frequency. These intermediaries will now be discussed in more detail.

4.1. Ionospheric Propagation

As stated in section 1, the morphology of the ionosphere can be considered the most important factor in HF radio propagation. When a signal is transmitted, it will take all paths made available by the antenna pattern. However, the majority of the signal will follow the path of least resistance, which is determined by the structure of the ionosphere. Figure 7 shows the groundscatter reflection location (gray histograms) and median VTEC (black circles) across all beams as functions of range gate (where the front field of view spans the positive range gates and the rear field of view spans the negative range gates) for December at noon (a) and midnight (b). Each plot within Figures 7a and 7b shows a different year, starting in 1999 (during the ascending phase of the 23rd solar cycle) when sufficient VTEC observations were available. The scatter bars on the VTEC show the interquartile range, meaning that the black circle represents the typical column-integrated electron density at that range gate, with the scatter bar denoting the azimuthal variation across the field of view. Because the azimuthal width of the radar beam increases with increasing distance from the radar, larger scatter bars closer to the radar denote the presence of greater horizontal density gradients than a similarly sized scatter bar further away from the radar. The groundscatter histograms are all scaled to show the percentage relative to each year's maximum groundscatter count for a single range gate at that season and local time (N_{max} , given at the top of each plot). This scaling makes it easier to identify the most probable groundscatter reflection location and compare the relative amount of groundscatter returning from each field of view in a given year.

Figure 7a shows that there is little variation in the location of groundscatter reflection points in either field of view, suggesting that there are no significant long-term changes in the availability of suitable reflection points over the solar cycle. This figure also shows a strong preference for groundscatter returning from the front field of view when the VTEC behind the radar is greater than 15 TECU. Because groundscatter preferentially returns from the front field of view regardless of the amount of VTEC or the level of spatial structure present in the ionospheric plasma density, it follows that the transmission frequencies used by Hankasalmi in common mode operations are most appropriate for the plasma density levels seen in front of the radar. The higher plasma density behind the radar causes greater refraction, limiting the available groundscatter paths. Years when the difference between the VTEC between the radar and the histogram maxima are large (such as in 2001, where this difference is on the order of 20 TECU and the rear maxima is located near range gate -20) see much less groundscatter from behind the radar than years when this difference is smaller (such as 1999 and 2002, when this difference is on the order of 10 TECU).

When the VTEC behind the radar drops sufficiently low in 2004, the difference in the VTEC between the front and rear histogram maxima decreases to the order of several TECU and the amount of groundscatter returning from behind the radar grows to about 40% of N_{max} . The rear field-of-view peak increases in 2005 and 2006 as the VTEC behind the radar decreases. This is consistent with the solar cycle variation seen in the $F:R$ for groundscatter in this temporal sector in Figures 4–6. The decrease in EUV irradiance as the solar cycle approaches solar minimum causes a decrease in the ionospheric plasma density, affecting the preferred direction for groundscatter propagation at Hankasalmi. In 2007 the percentage of groundscatter returning from behind the radar suddenly increased to about double that returning from the front field of view. This increase was caused by a decrease in the amount of groundscatter returning from in front of the radar rather than an increase in groundscatter returning from the rear field of view and occurs even though there is little change in the VTEC between 2006 and 2007. The two distinct peaks in the front field of view are due to the introduction of a second, higher transmission frequency.

At noon in December, Hankasalmi used only a transmission frequency band of 11.075–11.275 MHz in 2006. However, in 2007 an additional frequency band of 12.370–12.415 MHz was introduced. At this higher frequency band, groundscatter is expected to return from more distant range gates, since these rays are refracted less than the lower frequency band under the same ionospheric conditions. Because higher frequencies undergo less ionospheric refraction, they are less likely to return groundscatter; thus, the difference between

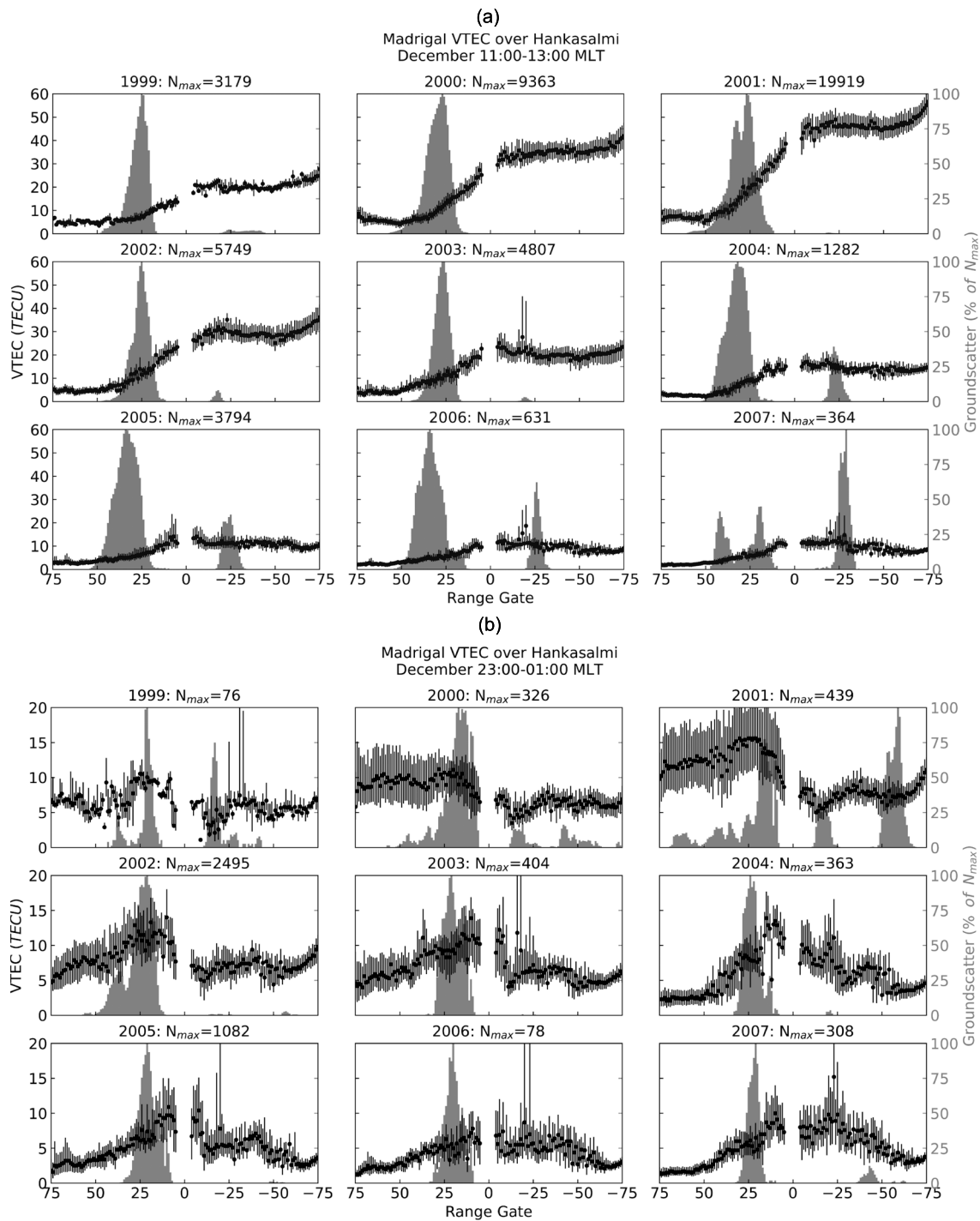


Figure 7. Median vertical total electron content (VTEC; black circles) and scaled groundscatter occurrence (gray histograms) over all beams as a function of range gate for the front (positive range gate) and rear (negative range gate) field of view. Each panel shows a different year for magnetic noon (a) and midnight (b) in December.

2006 and 2007 can be attributed to the introduction of a transmission frequency that is less likely to produce groundscatter at the 2007 ionospheric plasma density levels.

The diurnal variations in March, June, and September can also be explained by the daily change in ionospheric plasma density. These variations are presented in Figures 8–10, which show the median VTEC and distribution of groundscatter across all beams as a function of range gate for both magnetic noon (a) and magnetic

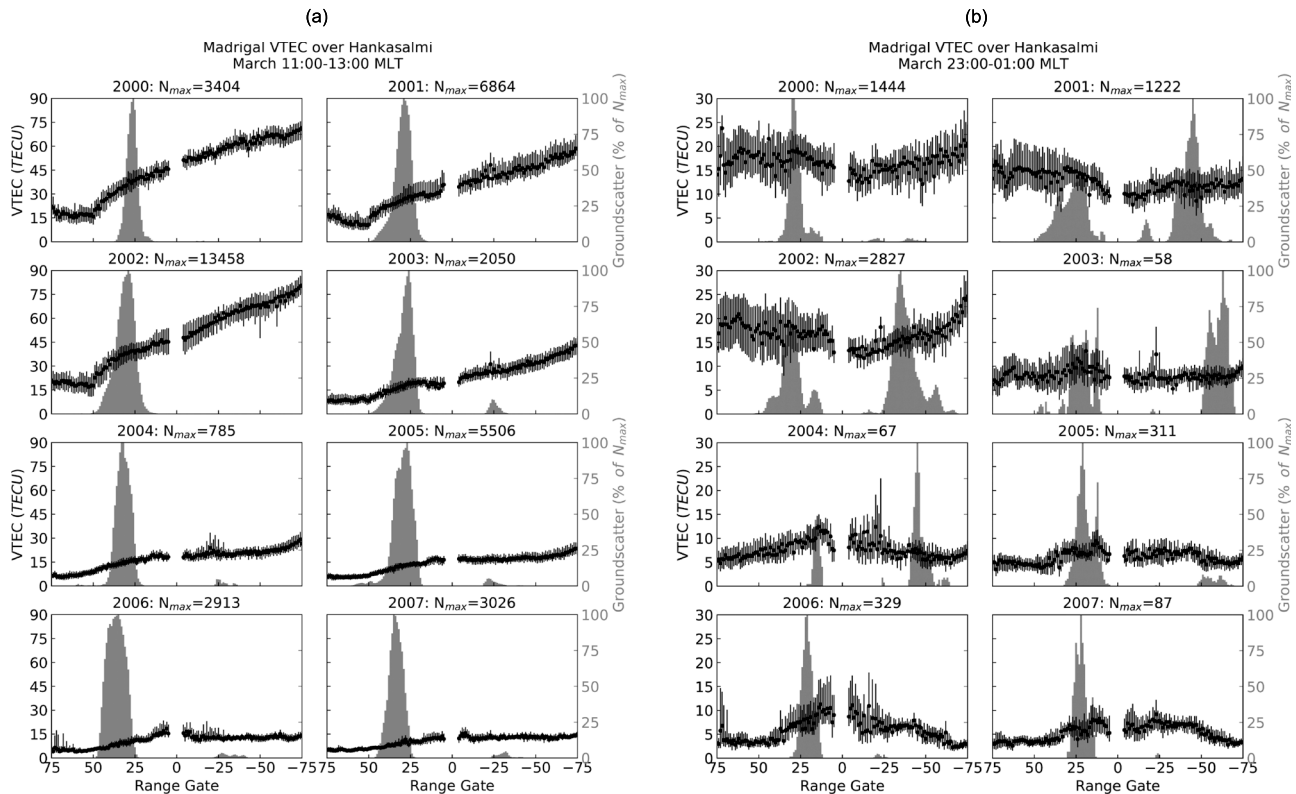


Figure 8. Median vertical total electron content (VTEC; black circles) and scaled groundscatter occurrence (gray histograms) over all beams as a function of range gate for the front (positive range gate) and rear (negative range gate) field of view. Each panel shows a different year for magnetic noon (a) and midnight (b) in March.

midnight (b) for March, June, and September, respectively. Figures 8–10 show that the daytime VTEC is always higher behind the radar than in front of the radar and that nearly all of the daytime groundscatter returns from the front field of view. At night, however, the VTEC behind the radar has similar magnitudes to that seen in front of the radar during the day. There are also less differences between the VTEC magnitudes in each field of view at night, increasing the likelihood of groundscatter returning from the rear field of view (especially if the transmission frequency was not adjusted to account for diurnal variations in the plasma density).

The presence of a solar cycle variation in the magnetic midnight sector for the equinox months seen in Figures 5 and 6 can also be seen in Figures 8b and 10b. The latter two figures show that groundscatter from the rear field of view becomes less frequent in 2005, when the VTEC between the radar and the groundscatter return location drops to levels typically below 8 TECU. During June in this magnetic local time sector, the VTEC never drops below this threshold, and no solar activity variation is seen in the groundscatter return direction.

The behavior of the preferred groundscatter return direction at midnight in December can also be explained by the ionospheric plasma density distribution. Unlike the other seasons, which are characterized by a relatively smooth decrease in ionospheric plasma density as latitude increases, the midlatitude trough (e.g., Scali, 1992) is located over Hankasalmi at night in December. Figure 7b shows the median VTEC and distribution of groundscatter across all beams as a function of range gate for midnight in December, while Figure 11 shows the median VTEC mapped over Europe with the groundscatter reflection locations shown for each field of view as a two-dimensional histogram. The solar maximum year 2001 shows a very clear example of the midlatitude trough. The poleward enhancement in plasma density can be seen to peak just north of the Norwegian coastline in the front field of view, around range gate 25, in Figure 11c. The density trough extends southward from Hankasalmi over Europe, with the equatorward density enhancement forming at the end of the rear field of view (over the Mediterranean Sea and northern Africa). The location of the midlatitude trough does not change with solar activity (Yang et al., 2015), consistent with the VTEC shown in Figures 7b and 11. However, the strength of the poleward enhancement does change over the solar cycle, decreasing as solar activity decreases.

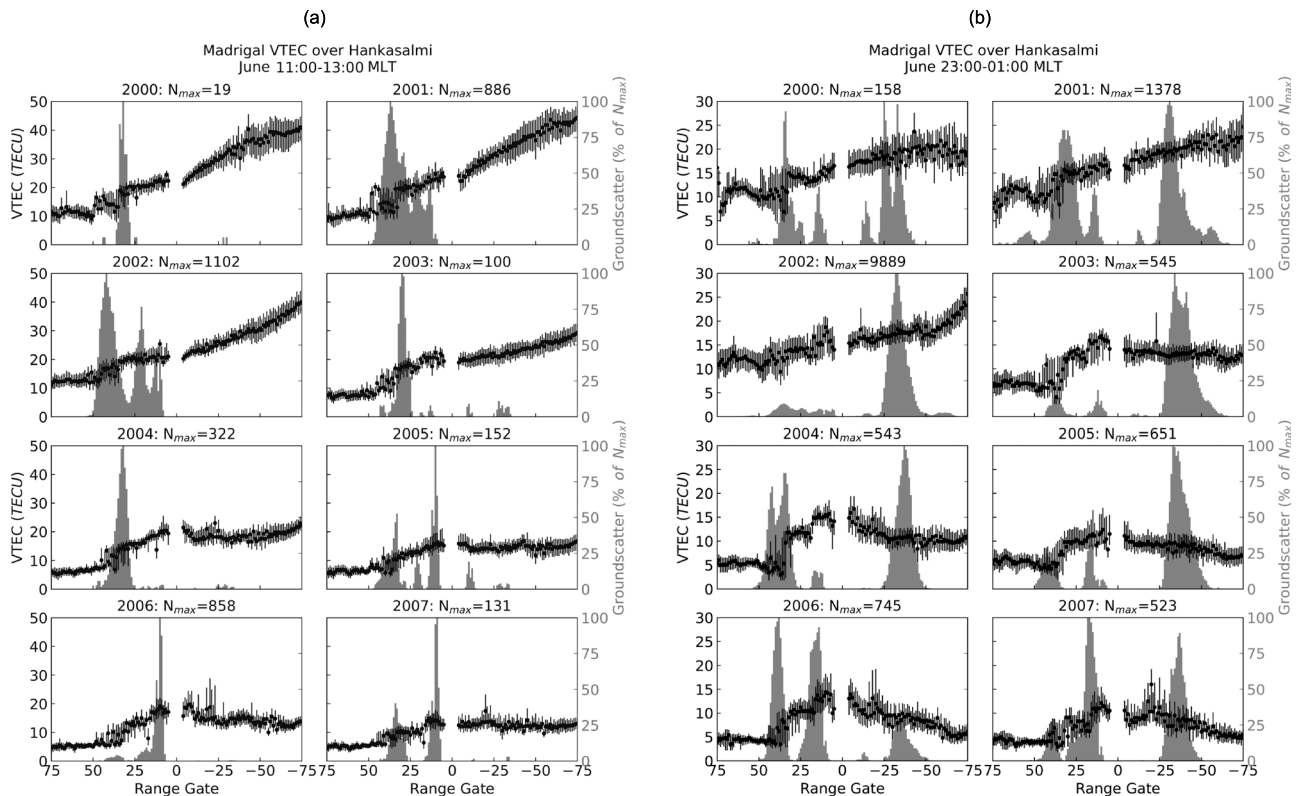


Figure 9. Median vertical total electron content (VTEC; black circles) and scaled groundscatter occurrence (gray histograms) over all beams as a function of range gate for the front (positive range gate) and rear (negative range gate) field of view. Each panel shows a different year for magnetic noon (a) and midnight (b) in June.

The poleward enhancement typically provides a more desirable propagation environment than the trough. Between 1999 and 2007, the VTEC in the poleward enhancement was over 8 TECU. The only year that the poleward enhancement does not improve groundscatter propagation in the front field of view is 2001, at solar maximum. This year has the highest VTEC across the entire rear field of view, and is the only year in this temporal sector to show more groundscatter returning from behind the radar than in front of the radar.

4.2. Sea Ice

Like all backscatter, groundscatter occurrence is affected by the presence of quality scattering targets. Backscatter will occur when the HF signal encounters a repetitive rough patch with a spatial separation that matches the half-wavelength of the probing signal. Appropriate irregularities are readily available on the ground in the form of mountains, rough sea (especially along coastlines), etc.

Sea ice is a poor scattering target. HF signals will propagate through the surface of the ice and dissipate. Because sea ice forms readily along coastlines at polar latitudes, it can affect the seasonal and long-term behavior of groundscatter observed by a high-latitude radar (Ponomarenko et al., 2010; Shand et al., 1998). Figure 12 shows the Equal Area Scalable Earth Grid 2.0 weekly snow cover and sea ice over the area covered by Hankasalmi's front and rear fields of view for the solar minimum years 1996 (a) and 2007 (f). Each field of view has black grid lines marking the 25th and 50th range gates, as well as purple and red bars highlighting beams 2 and 10, respectively. Both plots show that in December, only range gates greater than 30 in the front field of view are affected by sea ice. There is a long-term change in the distribution of sea ice; as time progresses less sea ice is observed (Barry, 2016). For example, the arm of ice seen around range gate 40 in beams 0–3 in 1996 is absent in 2007, and the southward extent of sea ice along the southern coast of Svalbard (the island covered by beam 10 near range gate 45) is greater in 1996 than in 2007. If the sea ice coverage plays a significant role in determining the December groundscatter return direction, the groundscatter occurrence in affected range gates should be higher in 2007 than in 1996.

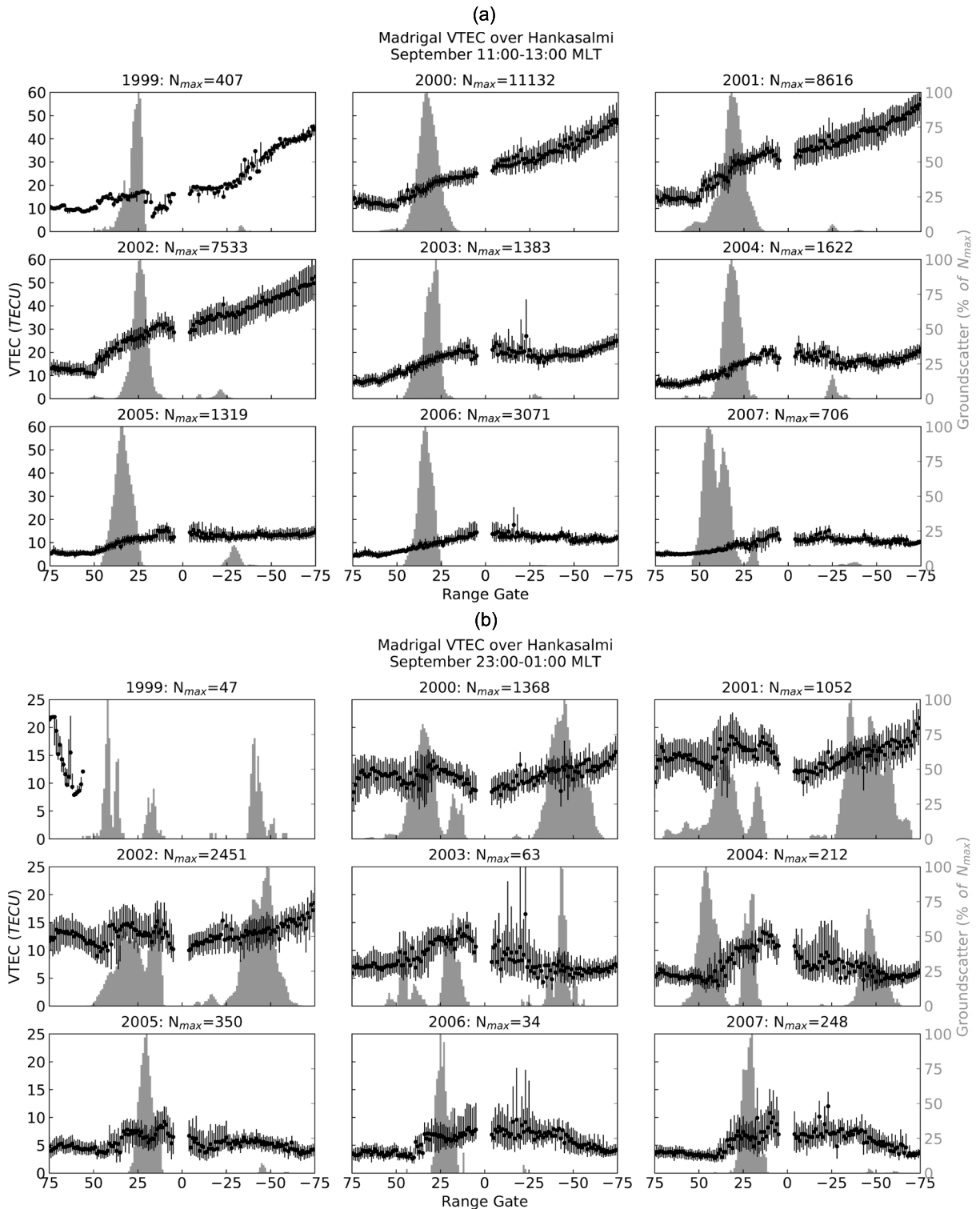


Figure 10. Median vertical total electron content (VTEC; black circles) and scaled groundscatter occurrence (gray histograms) over all beams as a function of range gate for the front (positive range gate) and rear (negative range gate) field of view. Each panel shows a different year for magnetic noon (a) and midnight (b) in September.

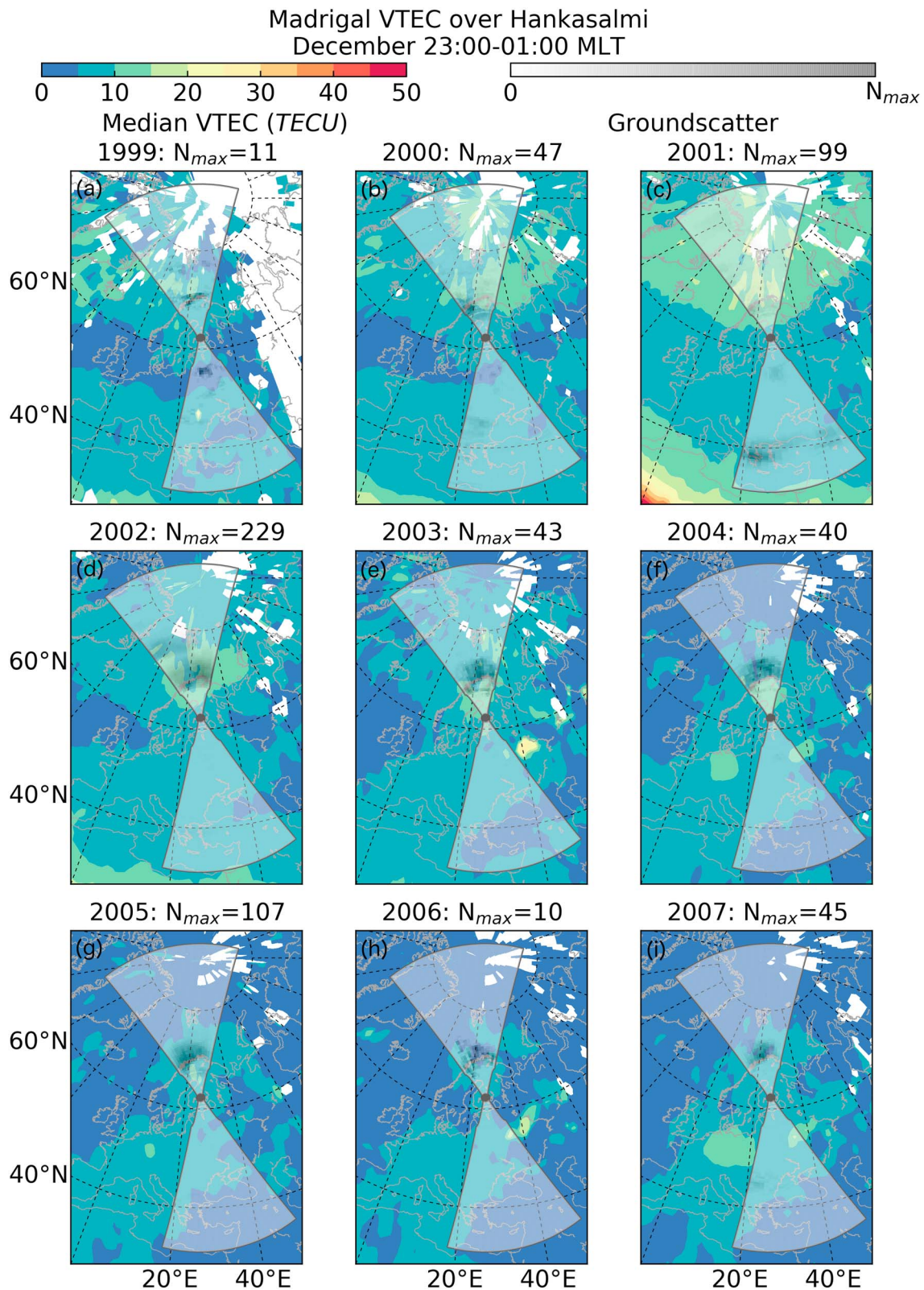


Figure 11. Median vertical total electron content (VTEC) plotted behind scaled groundscatter occurrence (grayscale fans) over all beams and range gates for the front (northward) and rear (southward) fields of view. Each panel shows a different year for magnetic midnight in December. In this figure, N_{max} is the maximum number of groundscatter observations for a single beam and range gate for each year at this season and local time.

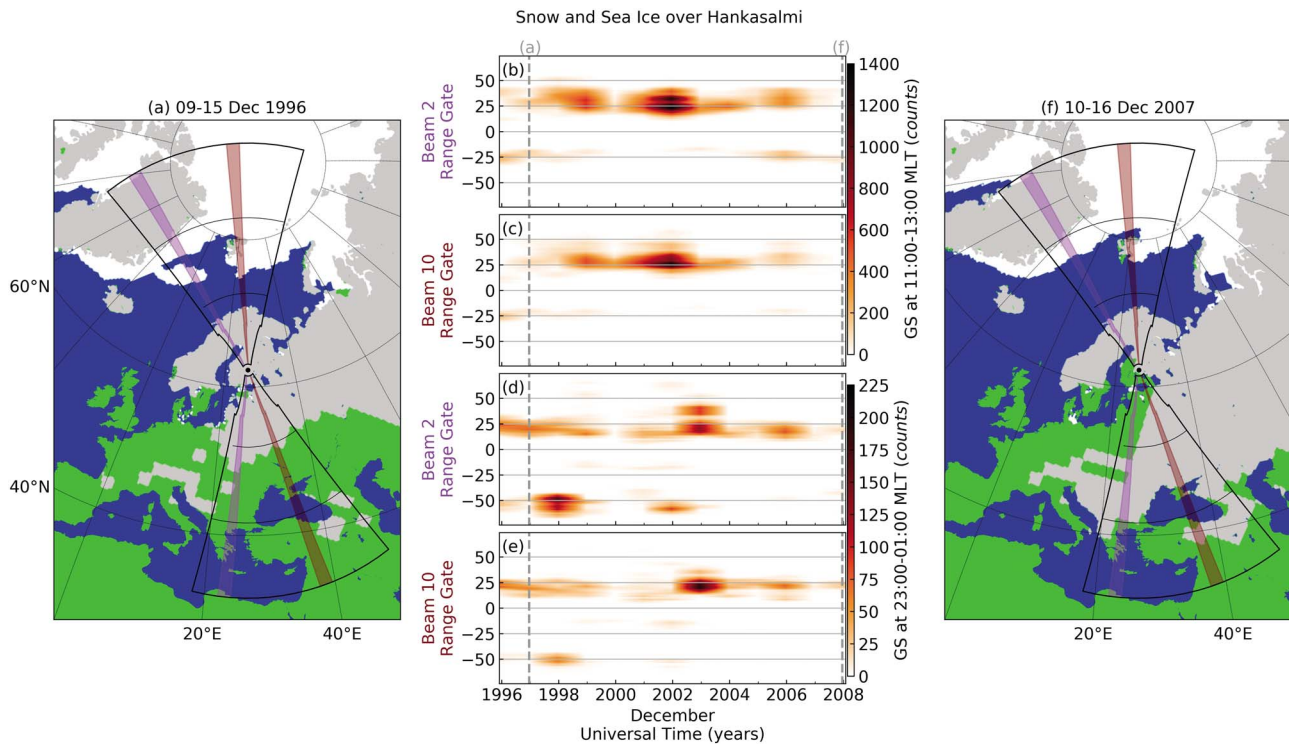


Figure 12. Sea ice (white) and snow (gray) maps over the Hankasalmi fields of view for 1996 (a) and 2007 (f) with groundscatter occurrence as a function of range gate and year (b–e) for beams 2 (purple) and 10 (red); range gates are gridded at 25 gate increments. Noon is shown in panels (b) and (c), and midnight in panels (d) and (e).

Figures 12b–12e show the December groundscatter distribution for beams 2 and 10 as a function of range gate and year for magnetic noon (b and c) and magnetic midnight (d and e). The dashed gray lines highlight the two years shown in panels (a) and (f). The influence of sea ice is seen most clearly in Figure 12b near range gates 30–35 in 1996, where the location of the arm of sea ice shown in panel (a) matches the hole in the groundscatter counts between range gates 25 and 40.

Despite the presence of this sea ice signature in the groundscatter, these plots show that the groundscatter returning from the front field of view is typically limited to the northern edge of the Scandinavian Peninsula, near range gate 25, and shows no expansion in range gate coverage as the sea ice retreats. At both local time sectors the ionospheric plasma density north of range gate 25 decreases rapidly in December, providing a propagation environment that produces little of the signal refraction necessary for groundscatter (as discussed in section 4.1 and shown in Figures 7 and 11). Thus, over the 23rd solar cycle, the structure of the ionosphere inhibited the necessary propagation conditions that would have allowed for a reduction in sea ice coverage to play a significant role in the groundscatter distribution at Hankasalmi.

4.3. Frequency Dependence

The radar program modes used to obtain the groundscatter statistics described above transmitted on four different frequency bands. These frequencies were selected to optimize the instances of ionospheric backscatter, assuming all ionospheric backscatter returns from the front field of view and so change with local time and solar activity. Figure 13 shows the percentage of groundscatter returning from each field of view for the four transmission frequency bands for each season and MLT division. All but the highest transmission frequency band detected groundscatter in all of the seasonal and MLT divisions and observed groundscatter returning from both fields of view.

It is clear that lower transmission frequencies observe a higher percentage of groundscatter from behind the radar at Hankasalmi. The trend for lower frequencies to return more groundscatter from the rear field of view than higher frequencies may be because their $F_p:R_p$ is lower. Another possible reason for this trend is that ionospheric propagation conditions behind the radar are typically more suitable for lower transmission

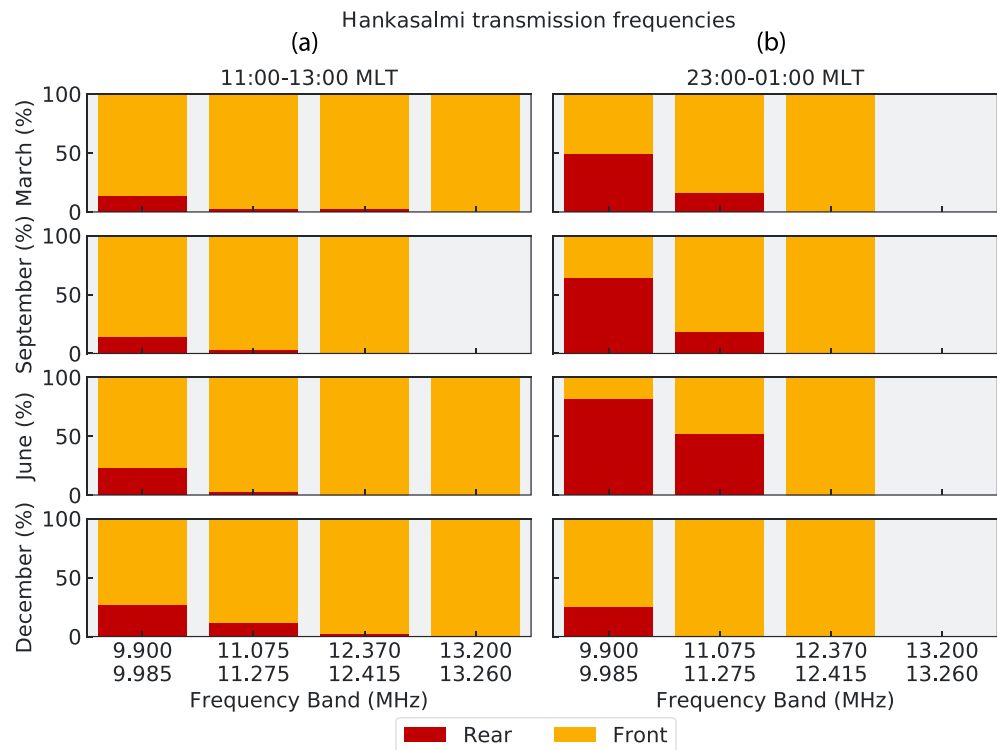


Figure 13. Percentage of backscatter returning from the front and rear fields of view for each season, magnetic local time (MLT), and transmission frequency, with noon in column (a) and midnight in column (b).

frequencies. Recall that Figure 2 shows that the amount of power directed behind the radar at all frequencies is large enough to return measurable backscatter, even when the $F_p:R_p$ is high.

The results presented in section 4.1 and Figure 7a indicate that both the $F_p:R_p$ and the ionospheric plasma density play a role in determining the relative occurrence of groundscatter in Hankasalmi's front and rear fields of view. For December 2007 near noon, the 11.075–11.275 MHz frequency band had a groundscatter $F:R = 1.006$ and the 12.370–12.415 MHz frequency band had a groundscatter $F:R = 2.132$. The decrease in the amount of backscatter returning from the rear field of view from about 50% in the lower frequency band to about 32% in the higher frequency band demonstrates the importance of the $F_p:R_p$, since the higher density of the ionospheric plasma behind the radar at this time is more conducive to groundscatter propagation at the 12.370–12.415 MHz frequency band than the ionospheric plasma density in front of the radar. Thus, both the $F_p:R_p$ and the ionospheric propagation conditions play a role in the groundscatter $F:R$.

5. Conclusions

Coherent-scatter, HF, phased-array radars can receive backscatter from both the primary beam and leakage behind the radar. Characterizing the front and rear lobe of each radar beam is challenging, since the radar transmission frequency, hardware, and local environmental conditions all play important roles. This study examined the relative occurrence of groundscatter from the front and rear fields of view over the 23rd solar cycle at the Hankasalmi SuperDARN radar.

During standard operations, the Hankasalmi radar was seen to observe groundscatter from both fields of view. Most groundscatter returned from the front field of view, but when ionospheric conditions provided a better propagation environment for groundscatter behind the radar (as commonly seen near magnetic midnight in June), groundscatter was more likely to return from the rear field of view. Because the ionospheric structure is of paramount importance in determining the groundscatter return direction, diurnal, seasonal, and solar cycle variations are present in the percentage of groundscatter returning from each field of view.

Coordinated experiments between the Hankasalmi radar and e-POP RRI were performed to elucidate the strength of the front and rear lobes. These experiments revealed that the majority of the transmitted power

Acknowledgments

A. G. Burrell, S. E. Milan, and T. K. Yeoman were supported by NERC grant NE/K011766/1. The research at the University of Calgary was supported by the Natural Sciences and Engineering Research Council of Canada (NSERC) Discovery Grant Program and Discovery Accelerator Supplement Program. The development and operations of the CASSIOPE/e-POP mission were supported by the Industrial Technologies Office (ITO), Canadian Space Agency (CSA), and MacDonald, Dettwiler and Associates (MDA), respectively. R. Stoneback was supported by NSF grant 1259508. e-POP RRI data can be accessed at <http://epop-data.phys.ucalgary.ca>. The authors acknowledge the use of IDL GEOPACK DLM in the production of the RRI data products used in this work. The authors acknowledge the use of SuperDARN data. SuperDARN is a collection of radars funded by the national scientific funding agencies of Australia, Canada, China, France, Italy, Japan, Norway, South Africa, the United Kingdom, and the United States. The Virginia Tech SuperDARN database (described at <http://vt.superdarn.org/>) provides up-to-date public access to the Hankasalmi observations, which were analyzed with the aid of DaViTpy. We acknowledge use of NASA/GSFC's Space Physics Data Facility's OMNI-Web service and OMNI data. Galactic Cosmic Ray data were obtained from the Sodankyla Geophysical Observatory at <http://cosmicrays oulu.fi>. GPS TEC data products and access through the Madrigal distributed data system are provided to the community by the Massachusetts Institute of Technology under support from U.S. National Science Foundation grant AGS-1242204. Data for the TEC processing is provided by the following organizations: UNAVCO, Scripps Orbit and Permanent Array Center, Institut Geographique National, France, International GNSS Service, The Crustal Dynamics Data Information System (CDDIS), National Geodetic Survey, Instituto Brasileiro de Geografia e Estatística, RAMSAC CORS of Instituto Geográfico Nacional del la República Argentina, Arecibo Observatory, Low-Latitude Ionospheric Sensor Network (LISN), Topcon Positioning Systems, Inc., Canadian High Arctic Ionospheric Network, Institute of Geology and Geophysics, Chinese Academy of Sciences, China Meteorology Administration, Centro di Ricerche Sismologiche, Système d'Observation du Niveau des Eaux Littorales (SONEL), RENAG : REseau National GPS permanent, and GeoNet—the official source of geological hazard information for New Zealand.

was sent into the front lobe, with a small percentage leaking out behind the radar at all transmitted frequencies. The front-to-rear power ratio was found to increase with increasing frequency. However, at all frequencies the amount of power seen behind the radar was sufficient to allow backscatter to return, provided there were appropriate scattering targets and an ionosphere suitable for groundscatter propagation at the transmitted frequency in the rear field of view.

References

- Alishouse, J. C. (1991). DMSP special sensor microwave/imager calibration/validation (Tech. Rep.) Washington, DC: Radio/IR/Optical Sensors Branch, Naval Research Laboratory.
- Barry, R. G. (2016). The Arctic cryosphere in the twenty-first century. *Geographical Review*, 107(1), 69–88. <https://doi.org/10.1029/2003JD003530>
- Blanchard, G. T., Sundeen, S., & Baker, K. B. (2009). Probabilistic identification of high-frequency radar backscatter from the ground and ionosphere based on spectral characteristics. *Radio Science*, 44, RS5012. <https://doi.org/10.1029/2009RS004141>
- Brodzik, M. J., & Armstrong, R. (2017). Northern Hemisphere EASE-Grid 2.0 Weekly Snow Cover and Sea Ice Extent, Version 4, NASA National Snow and Ice Data Center Distributed Arctic Archive Center. <https://doi.org/10.5067/P700HGJLYUQU>
- Burrell, A. G., Milan, S. E., Perry, G. W., & Yeoman, T. K. (2015). Automatically determining the origin direction and propagation mode of high-frequency radar backscatter. *Radio Science*, 50, 1225–1245. <https://doi.org/10.1002/2015RS005808>
- Burrell, A. G., Yeoman, T. K., Milan, S. E., & Lester, M. (2016). Phase calibration of interferometer arrays at high-frequency radars. *Radio Science*, 51, 1445–1456. <https://doi.org/10.1002/2016RS006089>
- Cane, H. V., Wibberenz, G., Richardson, I. G., & von Rosenvinge, T. T. (1999). Cosmic ray modulation and the solar magnetic field. *Geophysical Research Letters*, 26(5), 565–568. <https://doi.org/10.1023/A:1005083109827>
- Chisham, G., Lester, M., Milan, S. E., Freeman, M. P., Bristow, W. A., Grocott, A., et al. (2007). A decade of the Super Dual Auroral Radar Network (SuperDARN): Scientific achievements, new techniques and future directions. *Surveys in Geophysics*, 28(1), 33–109. <https://doi.org/10.1007/s10712-007-9017-8>
- Chisham, G., Yeoman, T. K., & Sofko, G. J. (2008). Mapping ionospheric backscatter measured by the SuperDARN HF radars Part 1: A new empirical virtual height model. *Annales Geophysicae*, 26(4), 823–841. <https://doi.org/10.5194/angeo-26-823-2008>
- Cortie, A. L. (1912). Sun-spots and terrestrial magnetic phenomena, 1898–1911. *Monthly Notices of the Royal Astronomical Society*, 73, 52. <https://doi.org/10.1093/mnras/73.1.52>
- Greenwald, R. A., Baker, K. B., Dudeney, J. R., Pinnock, M., Jones, T. B., Thomas, E. C., et al. (1995). DARN/SUPERDARN. *Space Science Reviews*, 71(1–4), 761–796. <https://doi.org/10.1007/BF00751350>
- Hall, G. E., MacDougall, J. W., Moorcroft, D. R., St Maurice, J. P., Manson, A. H., & Meek, C. E. (1997). Super dual auroral radar network observations of meteor echoes. *Journal of Geophysical Research*, 102(A7), 14,603–14,614. <https://doi.org/10.1029/97JA00517>
- Hargreaves, J. K. (1994). *The solar-terrestrial environment, Cambridge Atmospheric and Space Science Series* (Vol. 5). New York: Cambridge University Press.
- James, H. G., King, E. P., White, A., Hum, R. H., Lunscher, W. H. H. L., & Siefiring, C. L. (2015). The e-POP Radio Receiver Instrument on CASSIOPE. *Space Science Reviews*, 189(1), 79–105. <https://doi.org/10.1007/s11214-014-0130-y>
- Johannessen, O. M., Miles, M. W., & Bjorgo, E. (1996). Global sea ice monitoring from microwave satellites, in IGARSS. *International Geoscience and Remote Sensing Symposium, IEEE*, 96, 932–934. <https://doi.org/10.1109/IGARSS.1996.516525>
- Liu, L. B., Wan, W., Chen, Y., & Le, H. (2011). Solar activity effects of the ionosphere: A brief review. *Chinese Science Bulletin*, 56(12), 1202–1211. <https://doi.org/10.1007/s11434-010-4226-9>
- Milan, S. E., Yeoman, T. K., Lester, M., Thomas, E. C., & Jones, T. B. (1997). Initial backscatter occurrence statistics from the CUTLASS HF radars. *Annales Geophysicae*, 15(6), 703–718. <https://doi.org/10.1007/s00585-997-0703-0>
- Milan, S. E., Jones, T. B., Robinson, T. R., Thomas, E. C., & Yeoman, T. K. (1997). Interferometric evidence for the observation of ground backscatter originating behind the CUTLASS coherent HF radars. *Annales Geophysicae*, 15(1), 29–39. <https://doi.org/10.1007/s00585-997-0029-y>
- Perry, G. W., James, H. G., Gillies, R. G., Howarth, A., Hussey, G. C., McWilliams, K. A., et al. (2017). First results of HF radio science with e-POP RRI and superDARN. *Radio Science*, 52, 78–93. <https://doi.org/10.1002/2016RS006142>
- Ponomarenko, P. V., & Waters, C. L. (2006). FITACF description and revision. Retrieved from https://homepage.usask.ca/~pbp672/FITACF_Newcastle.pdf
- Ponomarenko, P. V., St Maurice, J. P., Hussey, G. C., & Koustov, A. V. (2010). HF ground scatter from the polar cap: Ionospheric propagation and ground surface effects. *Journal of Geophysical Research*, 115, A10310. <https://doi.org/10.1029/2010JA015828>
- Ponomarenko, P. V., Nishitani, N., Oinats, A. V., Tsuya, T., & Maurice, J.-P. S. (2015). Application of ground scatter returns for calibration of HF interferometry data. *Earth Planets Space*, 67, 1–9. <https://doi.org/10.1186/s40623-015-0310-3>
- Ponomarenko, P. V. (2017). On the presence of Type 1 echoes in SuperDARN data. In *SuperDARN Workshop*. San Quirico D'Orcia, Italy.
- Ribeiro, A. J., Ruohoniemi, J. M., Baker, J., Clausen, L. B. N., de Larquier, S., & Greenwald, R. A. (2011). A new approach for identifying ionospheric backscatter in midlatitude SuperDARN HF radar observations. *Radio Science*, 46, RS4011. <https://doi.org/10.1029/2011RS004676>
- Rideout, W., & Coster, A. J. (2006). Automated GPS processing for global total electron content data. *GPS Solutions*, 10(3), 219–228. <https://doi.org/10.1007/s10291-006-0029-5>
- Ruohoniemi, J. M., & Baker, K. B. (1998). Large-scale imaging of high-latitude convection with Super Dual Auroral Radar Network HF radar observations. *Journal of Geophysical Research*, 103, 20,797–20,811.
- Scali, J. L. (1992). The mid-latitude trough (Tech. Rep. 2). Lowell, Lexington MA: University of Massachusetts.
- Shand, B. A., Milan, S. E., Yeoman, T. K., Chapman, P. J., Wright, D. M., Jones, T. B., & Pedersen, L. T. (1998). CUTLASS HF radar observations of the Odden ice tongue. *Annales Geophysicae - Atmospheres Hydrospheres and Space Sciences*, 16(2), 280–282.
- Shepherd, S. G. (2014). Altitude-adjusted corrected geomagnetic coordinates: Definition and functional approximations. *Journal of Geophysical Research: Space Physics*, 119, 7501–7521. <https://doi.org/10.1002/2014JA020264>
- Sterne, K. T., Greenwald, R., Baker, J. B. H., & Ruohoniemi, J. M. (2011). Modeling of a twin terminated folded dipole antenna for the Super Dual Auroral Radar Network (SuperDARN). In *Radar Conference (RADAR)* (pp. 934–938). Kansas City. <https://doi.org/10.1109/RADAR.2011.5960673>
- SuperDARN Data Analysis Working Group Participating members, Thomas, E. G., Ponomarenko, P. V., Bland, E. C., Burrell, A. G., Kotyk, K., et al. (2018). SuperDARN Radar Software Toolkit (RST) (Version 4.1), Zenodo. <https://doi.org/10.5281/zenodo.1143675>

- Usoskin, I. G., Mursula, K., Kangas, J., & Gvozdevsky, B. (2001). On-line database of cosmic ray intensities. In *Proceedings of ICRC* (pp. 1–4). Hamburg, Germany.
- Werner, S., & Pröls, G. W. (1997). The position of the ionospheric trough as a function of local time and magnetic activity. *Advances in Space Research*, 20(9), 1717–1722.
- Yang, N., Le, H., & Liu, L. (2015). Statistical analysis of ionospheric mid-latitude trough over the Northern Hemisphere derived from GPS total electron content data. *Earth Planets Space*, 67, 1–11. <https://doi.org/10.1186/s40623-015-0365-1>
- Yau, A. W., & James, H. G. (2015). CASSIOPE Enhanced Polar Outflow Probe (e-POP) mission overview. *Space Science Reviews*, 189(1), 3–14. <https://doi.org/10.1007/s11214-015-0135-1>
- Yeoman, T. K., Wright, D. M., Stocker, A. J., & Jones, T. B. (2001). An evaluation of range accuracy in the Super Dual Auroral Radar Network over-the-horizon HF radar systems. *Radio Science*, 36(4), 801–813. <https://doi.org/10.1029/2000RS002558>